High-Q UHF Micromechanical Radial-Contour Mode Disk Resonators

John R. Clark, *Member, IEEE*, Wan-Thai Hsu, *Member, IEEE*, Mohamed A. Abdelmoneum, *Student Member, IEEE*, and Clark T.-C. Nguyen, *Senior Member, IEEE*

***Abstract*—A micromechanical, laterally vibrating disk resonator, fabricated via a technology combining polysilicon surface-micromachining and metal electroplating to attain submicron lateral capacitive gaps, has been demonstrated at frequencies as high as 829 MHz and with Q's as high as 23 000 at 193 MHz. Furthermore, the resonators have been demonstrated operating in the first three radial contour modes, allowing a significant frequency increase without scaling the device, and a 193 MHz resonator has been shown operating at atmospheric pressure with a Q of 8,880, evidence that vacuum packaging is not necessary for many applications. These results represent an important step toward reaching the frequencies required by the RF front-ends in wireless transceivers. The geometric dimensions necessary to reach a given frequency are larger for this contour-mode than for the flexural-modes used by previous resonators. This, coupled with its unprecedented Q value, makes this disk resonator a choice candidate for use in the IF and RF stages of future miniaturized transceivers. Finally, a number of measurement techniques are demonstrated, including two electromechanical mixing techniques, and evaluated for their ability to measure the performance of sub-optimal (e.g., insufficiently small capacitive gap, limited dc-bias), high-frequency, high-Q micromechanical resonators under conditions where parasitic effects could otherwise mask motional output currents. [1051]**

***Index Terms*—Electromechanical coupling, microelectromechanical systems (MEMS), microelectromechanical devices, microresonator, quality factor, resonator, UHF, VHF.**

NOMENCLATURE

α Empirical scaling factor for simplified resonance frequency calculations (dependent on the mode number).
d Electrode-to-resonator gap spacing.
d_o Static electrode-to-resonator gap spacing.
C_o Electrode-to-resonator static overlap capacitance. In circuit models only (but not in design equations), may also include additional parasitic capacitance.
C_x Port-to-port series motional capacitance in the condensed resonator equivalent circuit.
c_x Stiffness-equivalent internal series motional capacitance in the full (uncondensed) resonator equivalent circuit.
E Young's modulus of elasticity.
ε_o Free space permittivity ($= 8.854 \times 10^{-12}$ F/m).
F_{res} Amplitude of the force acting on a resonator.
f_o Resonance frequency of a mechanical resonator.
f_p Parallel resonance frequency generated by parasitic feedthrough.
η Electromechanical coupling coefficient.
i_o Output motional current.
$J_n(y)$ Bessel function of the first kind of order n.
κ Empirical fitting factor for simplified resonance frequency calculations—dependant on σ.
KE_{tot} Peak total kinetic energy.
k_{re} Radial-direction mechanical stiffness at a location on the disk perimeter.
L_x Port-to-port series motional inductance in the condensed resonator equivalent circuit.
l_x Mass-equivalent internal series motional inductance in the full (uncondensed) resonator equivalent circuit.
m_{re} Radial-direction equivalent mass of a disk resonator at a location on the disk perimeter.
σ Poisson's ratio.
ρ Density.
Q Unloaded quality factor.
$\Re$ Radial displacement amplitude at the disk perimeter.
R Radius of the disk resonator.
R_L Measurement load resistance.
R_x Port-to-port series motional resistance in the condensed resonator equivalent circuit.
r Displacement of the disk perimeter measured along the radius.
r_x Damping-equivalent internal series motional resistance in the full (uncondensed) resonator equivalent circuit.
t Disk resonator thickness.
$V(r)$ Radial velocity a distance r from the center of the resonator disk.
V_i Small signal input voltage amplitude.
v_i Small signal input voltage.
v_o Output voltage developed across R_L.
V_P Resonator dc-bias voltage.
V_x Amplitude of input voltage component x.
ω_c Carrier frequency for mixing measurements.
ω_o f_o in rad/s.

Manuscript received May 1, 2003; revised March 4, 2005. This work was supported by the Defense Advanced Research Projects Agency (DARPA) under Grant F30602-97-2-0101. Subject Editor G. K. Fedder.

J. R. Clark and W.-T. Hsu were with the Department of Electrical Engineering and Computer Science, University of Michigan, Ann Arbor, MI 48109-2212 USA. They are now with Discera, Inc., Ann Arbor, MI 48108 USA (e-mail: johnclark@discera.com; wanthaihsu@discera.com).

M. A. Abdelmoneum was with the Department of Electrical Engineering and Computer Science, University of Michigan, Ann Arbor, MI 48109-2212 USA. He is now with with Intel, Hillsboro, OR USA 97124 (e-mail: mohamed.a.abdelmoneum@intel.com).

C. T.-C. Nguyen is with the Department of Electrical Engineering and Computer Science, University of Michigan, Ann Arbor, MI 48109-2212 USA. He is also with DARPA, Arlington, VA 22203 USA (e-mail: ctnguyen@umich.edu).

Digital Object Identifier 10.1109/JMEMS.2005.856675

1057-7157/$20.00 © 2005 IEEE

I. Introduction

WITH recent frequency increases into the mid-VHF range [1]–[5], vibrating micromechanical ("μmechanical") resonators with Q's approaching 100 000 [4] have emerged as leading candidates for on-chip versions of the low-loss, small percent bandwidth IF filters and the high-Q reference oscillator tanks required in wireless communication handsets. Having achieved the VHF frequencies needed for IF applications, μmechanical resonators now look toward the UHF frequencies needed for RF applications. As detailed in [6], μmechanical resonators are projected to make their biggest impact in RF applications, as the defining elements in RF channel-select filter banks and ultra-low power, low-phase noise synthesizers, both made possible by Q's $>5,000$ and targeted for use in alternative transceiver architectures that trade power for Q.

Much like the case for transistors, extending the frequency of μmechanical resonators generally entails scaling of resonator dimensions. As a result, previous VHF demonstrations have used submicron dimensions to achieve higher frequencies—an approach that also reduced Q-limiting anchor losses by maintaining small values of resonator stiffness [1]. Unfortunately, smaller size often coincides with smaller power handling [7], [8] and an increased susceptibility to environmental effects [9], such as contamination or thermal fluctuations. Although recently demonstrated free-free beam μmechanical resonators have been able to achieve frequencies up to 92 MHz with Q's around 8000 while avoiding submicron dimensions [1], whether or not they can maintain their size and Q at UHF frequencies has yet to be seen.

This paper presents a comprehensive description of an alternative, perhaps superior, design based on the radial contour mode, or areal dilation, of a μmechanical disk structure [2] capable of attaining very high frequencies while retaining relatively large dimensions. Using this disk design, operating in the fundamental mode, a frequency of 433 MHz has been attained with a Q exceeding 4000 and a diameter of 12.6 μm—slightly larger than the length of 11.3 μm required to attain only 92 MHz in previous free-free beam resonators. Disk resonators have also been tested operating in the second and third overtones, yielding frequencies as high as 829 MHz. The resonators were evaluated using several different measurement techniques described and contrasted herein, including a novel electromechanical mixing measurement technique intended to reduce parasitic effects at the resonance frequency, resulting in a vast improvement in the accuracy of the extracted Q value over a typical direct measurement, and in some cases enabling a measurement where direct techniques could not detect the resonance signal.

II. Device Description and Operation

Fig. 1 presents the perspective-view schematic of the disk μresonator, identifying key dimensions and indicating a two-port bias and excitation scheme. The resonator consists of a disk suspended 500 nm above the substrate with a single anchor at its center. Plated metal input electrodes surround the perimeter of the disk, separated from the disk by a narrow air (or vacuum) gap that defines the capacitive, electromechanical transducer of this device. To operate the device, a dc bias voltage V_P is applied to the structure via interconnect to the stem, while an ac input signal is applied to the input electrode, resulting in a time varying electrostatic force acting radially on the disk. When the input signal, and hence the force that it generates, are acting at the resonance frequency of the device, the effect of that force is multiplied by the Q factor of the resonator, producing expansion and contraction of the disk along its radius, as shown Fig. 2, which illustrates the shape of the fundamental mode. This motion, in turn, results in a time-varying, dc-biased capacitor between the disk and the output electrode generating an output current given by

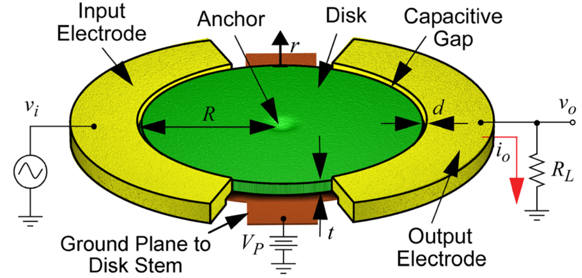

Fig. 1. Perspective view schematic of a disk micromechanical resonator illustrating a preferred two-port bias and excitation scheme. (Color version available online at http://ieeexlpore.ieee.org.)

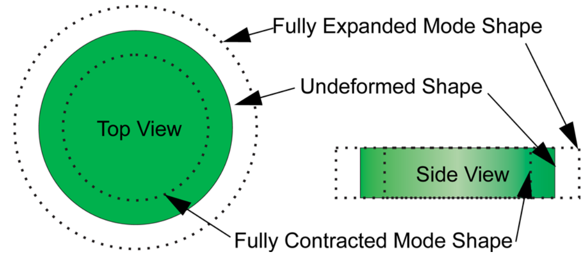

Fig. 2. The radial contour mode shape for the fundamental mode ideally exhibits no rotational or flexural components. (Color version available online at http://ieeexlpore.ieee.org.)

$$i_o = V_P \frac{\partial C_o}{\partial r} \frac{\partial r}{\partial t} \tag{1}$$

where r is the radial displacement at the edge of the disk and $\partial C_o/\partial r$ is the change in electrode-to-resonator sense capacitance per unit displacement. The output current i_o can be sensed either directly as the voltage across the load resistor R_L, or via a transimpedance amplifier. Note that if the mechanical resonator Q is the primary parameter to be measured, the load resistance R_L should be kept small in order to minimize Q-loading.

As indicated in Fig. 2, the radial contour mode constrains the vibration of the resonator entirely within the plane of the device with ideally no out-of-plane motion. In addition, the particular modes of this work exhibit no rotational motion around the centroid, leaving only extensional movement of the resonator mass and yielding a very high stiffness and frequency associated with longitudinal vibrations. An infinite number of higher overtones also exist which adhere to these restrictions. Fig. 3 illustrates the first three such modes, all of which are measured within this work. Arrows indicate direction of vibration throughout one half-cycle, and shaded contours indicate relative displacement. In the fundamental mode, the entire disk is moving in-phase along the radius, with maximum displacement at the edges and a stationary nodal point in the center. In addition to the central node, the second mode adds a nodal circumference at which the resonator is also stationary and the phase of vibration reverses. The third mode adds yet another nodal circumference, creating

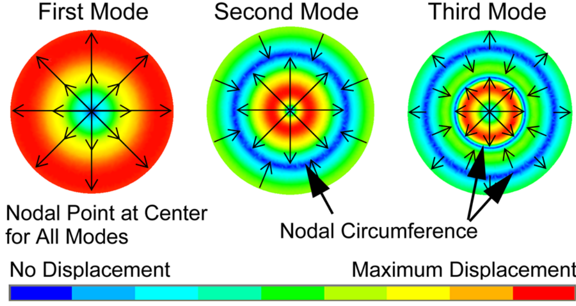

Fig. 3. Contour plots for a disk vibrating in the radial-contour mode up to third order with shading indicating the relative magnitude of displacement and arrows indicating the relative direction for each mode shape. (Color version available online at http://ieeexlpore.ieee.org.)

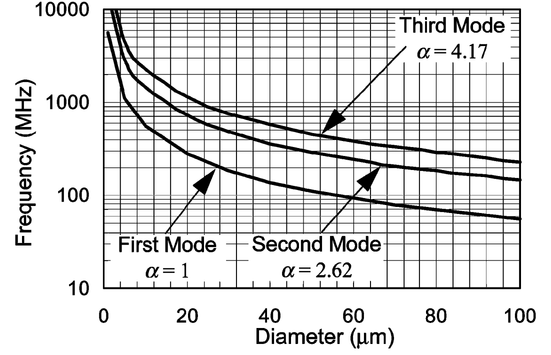

Fig. 4. Plot of frequency versus diameter for a polysilicon disk operating in the radial-contour mode.

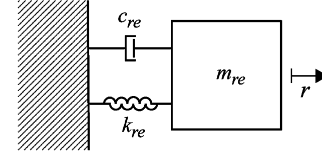

Fig. 5. Equivalent mass-spring-damper lumped mechanical model for a micromechanical disk resonator.

three distinct vibrating regions. Additional nth-order overtones are possible, with each mode having a central node and $n-1$ nodal circumferences.

Previous work on free-free beam μmechanical resonators has shown that resonators with relatively large dimensions exhibit higher stiffnesses than their submicron counterparts and thus can achieve high Q only if sufficiently isolated from the substrate so as to eliminate energy losses to it. In the particular free-free beam design of [1], isolation from the substrate was achieved in part by attaching support beams only at flexural-mode nodal points. The disk design of this work very conveniently allows a similar isolation strategy. In particular, because the motion of the disk is symmetric and purely radial at the desired resonance, anchoring the resonator at its central node, as shown in Fig. 1, minimizes energy losses to the substrate, allowing high-Q operation despite the high stiffness of the design.

III. Theory and Design

To facilitate the incorporation of disk resonators into filter and oscillator designs, equivalent models and analytical formulations for resonator properties (e.g., resonance frequency, impedance) are needed. These are addressed in Sections III-A–C.

A. Geometric Frequency Design

The mechanical resonance frequency for the radial contour mode of a disk is governed mainly by its material properties and radius. Neglecting second order effects due to thickness and finite anchor dimensions, the resonance frequency may be determined by finding a numerical solution for f_o to the system of equations [10]

$$\frac{\zeta}{\xi} \cdot \frac{J_0\left(\frac{\zeta}{\xi}\right)}{J_1\left(\frac{\zeta}{\xi}\right)} = 1 - \sigma \tag{2}$$

where

$$\zeta = 2\pi f_o R \sqrt{\frac{\rho(2+2\sigma)}{E}} \tag{3}$$

$$\xi = \sqrt{\frac{2}{1-\sigma}} \tag{4}$$

and where R is the radius of the disk; E, σ, and ρ are the Young's modulus, Poisson's ratio, and density, respectively, of its structural material; and $J_i(y)$ is the Bessel function of the first kind of order i. The solution to (2)–(4) is periodic, so that the frequency of the nth mode corresponds to the nth solution.

While representing a rigorous solution to the differential equations of vibration, this set of equations does not provide clear insight into how the individual parameters affect the frequency. By sacrificing some degree of accuracy, (2)–(4) can be rendered into the more intuitive form

$$f_o = \frac{\kappa\alpha}{R}\sqrt{\frac{E}{\rho}} \tag{5}$$

where κ is a parameter dependent upon Poisson's ratio ($\kappa = 0.342$ for polysilicon [11]) and α depends on the order of the desired mode. Fig. 4 shows the resonance frequency versus diameter for polysilicon disks, showing the inverse relationship between frequency and size. In addition, Fig. 4 gives the values of α for the first three modes. The advantage of using higher overtones is clear; a 1 GHz resonator operating in the first mode requires a diameter of 5.5 μm, while the second and third modes require 14.5 μm and 23.0 μm diameters respectively, helping to overcome potential lithography and power-handling issues as frequency scales. However, even in the fundamental mode, at the 900–1800 MHz RF frequencies commonly used in wireless handsets, the required diameters of 6.2 μm for 900 MHz and 3 μm for 1.8 GHz are well within the capabilities of present-day integrated circuit fabrication technology.

B. Equivalent Mechanical Model

As with any vibratory system, the disk resonator may be represented by a lumped-element equivalent mechanical model such as that depicted in Fig. 5. This model, composed of a rigid-body mass connected to a stationary base through spring and damper elements, aids in the design of more complex systems, such as filters, and serves as the basis for the electrical model described in the next section. The equivalent mass m_{re} at any given point on the perimeter of the disk is determined from the total kinetic energy in the resonator and the velocity at that point, as given by [11]

$$m_{re} = \frac{KE_{\text{tot}}}{\frac{1}{2}V(R)^2} = \frac{2\rho\pi t}{V(R)^2}\int_0^R rV(r)^2 \partial r = \frac{2\rho\pi t}{J_1(hR)^2}\int_0^R rJ_1(hr)^2 \partial r \tag{6}$$

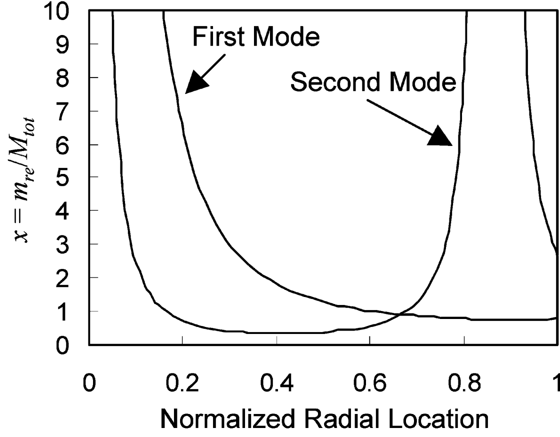

Fig. 6. Plot of the scale factor x relating the effective dynamic mass m_{re} to the total static mass $M_{\rm tot}$ of a disk, as a function of radial location on the disk normalized to the disk radius R.

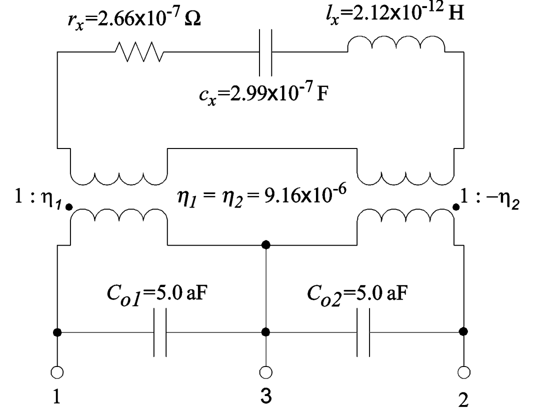

Fig. 7. Equivalent circuit model for a disk resonator with two ports. The model is comprised of an *RLC* tank to model the resonant behavior and transformers to model each port. Element values given correspond to the 13.7 μm-radius, 2 μm-thick disk resonator measured in Section VI, assuming $V_P = 30$ V.

where

$$V(r) = \omega_o h J_1(hr) \tag{7}$$

$$h = \sqrt{\frac{\omega_o^2 \rho}{\frac{2E}{2+2\sigma} + \frac{E\sigma}{1-\sigma^2}}} \tag{8}$$

and where $KE_{\rm tot}$ is the total peak kinetic energy in the vibrating system, $V(r)$ is the radial velocity of a point at a distance r from the center, t is the thickness of the disk, and $\omega_o = 2\pi f_o$. (The "e" notation in m_{re} indicates that the equivalent mass value corresponds to the electrode location, i.e., in this case, at the disk perimeter.) Note that if R is determined from (2)–(4), then no changes in (6)–(10) are necessary to account for higher order modes. To gain design intuition into the value of the effective dynamic mass $m_{\rm re}$, a simple expression relating its magnitude to the total static mass $M_{\rm tot}$ of a disk can be written as

$$m_{\rm re} = x M_{\rm tot} \tag{9}$$

where $M_{\rm tot} = \rho \pi R^2 t$. Using (6), Fig. 6 plots x as a function of normalized disk radial location (i.e., normalized to the disk radius) for the first mode and second modes, showing that, for the first mode, the equivalent mass is slightly less than the static mass at the edge of the resonator, but increases rapidly toward the center. For the second mode, an outer nodal ring is observed, where the mass ratio shows a peak near the edge.

The effective stiffness $k_{\rm re}$ at the perimeter of the disk resonator can be related to $m_{\rm re}$ via the radian resonance frequency ω_o to yield the expression

$$k_{\rm re} = \omega_o^2 m_{\rm re}. \tag{10}$$

For the 13.7 μm-radius, 2 μm-thick fundamental-mode disk measured later in Section VI, the effective stiffness k_{re} is 3.34 MN/m, which is substantially larger than the 2–80 kN/m posted by previous VHF micromechanical resonators.

Finally, the value of the damping element is related to both m_{re} and k_{re}, as well as the Q of the resonator, by

$$c_{re} = \frac{\sqrt{k_{re} m_{re}}}{Q}. \tag{11}$$

In most cases, the Q of the resonator is difficult to predict theoretically, so the damping element is typically determined empirically. Also, note that the effective mass and stiffness on the perimeter of a radial contour mode disk are independent of location, indicating that all points on the circumference of the disk are moving with the same velocity, obviating the complex integration required to obtain accurate model parameters in flexural mode resonator counterparts [12].

The primary output variable of the mechanical model is the displacement of the mass, which is equivalent to the radial displacement at the perimeter of the disk along its radius. The amplitude of the displacement at resonance is given by

$$\Re = \frac{QF_i}{k_{\rm re}} = \frac{Q}{k_{\rm re}} \cdot \frac{\partial C_o}{\partial r} \cdot V_p V_i = \frac{QC_o V_P V_i}{d_o k_{\rm re}} \tag{12}$$

where V_i is the amplitude of the ac input signal at the disk resonance frequency, d_o is the electrode-to-resonator gap, and C_o is the static electrode-to-resonator capacitance at the input port.

C. Equivalent Electrical Circuit Model

The mechanical model introduced in the previous section may be transformed into an equivalent electrical circuit of the form shown in Fig. 7, which presents an equivalent *RLC* circuit modeling the disk resonator of Fig. 1. In this circuit [12], the motional elements l_x, c_x, and r_x, model the resonant behavior of the device and are directly related to the mass-spring-damper values, respectively, by

$$l_x = m_r \tag{13}$$

$$c_x = \frac{1}{k_r} \tag{14}$$

$$r_x = c_r. \tag{15}$$

A transformer models the electromechanical transduction at each port, while the capacitor $C_{\rm on}$ models the capacitance between the nth port and the resonator body, consisting largely of the static capacitance between the electrode and disk but also including any additional parasitic capacitance between the ports and ac ground. Comparing Fig. 7 with Fig. 1, Port 1 corresponds to the input electrode, Port 2 corresponds to the output electrode, and Port 3 corresponds to the port where the dc-bias is applied to the structure. The transformer at each port n is characterized by an electromechanical coupling coefficient given by

$$\eta_n = V_P \frac{\partial C_{\rm on}}{\partial r}. \tag{16}$$

The negative sign in the turns ratio of the second port ensures the proper current directions in the resonance tank loop—i.e., if the

negative sign where omitted, an identical positive input voltage on Ports 1 and 2 would result in the currents canceling in the tank, which would contradict the displacement pattern of the disk when operating in the radial-contour mode. If the number of ports on the device differs from the two shown in Fig. 7, then a transformer may be added (or removed) for each additional (or eliminated) port. Care should be taken when adding ports to the model to ensure that the transformer currents sum at the body port (Port 3 in the figure) and in the resonant tank loop to avoid the aforementioned current cancellation.

In many applications, the series motional resistance looking into port n, designated R_{xn}, must be minimized for impedance matching purposes. R_{xn} is given by the impedance transformation of r_x

$$R_{xn} = \frac{r_x}{\eta_n^2} = \frac{c_{re}}{\eta_n^2}. \tag{17}$$

According to the (11), (16), and (17), and assuming that Q is fixed, this is best accomplished by maximizing the dc-bias voltage V_P and/or the $\partial C_{\text{on}}/\partial r$ term. In many practical systems, however, the maximum voltage is often limited by either the transistor technology supporting the resonator or the available power supply, leaving $\partial C_{\text{on}}/\partial r$, which varies as (t/d_o^2), as the only adjustable parameter. Thickness t is limited by technology constraints and by second order effects that cause frequency to decrease as thickness increases, so $\partial C_{\text{on}}/\partial r$ is best increased by decreasing the electrode-to-resonator gap spacing d_o. Since $\partial C_{\text{on}}/\partial r$ varies as $(1/d_o^2)$, changes in d_o have a very strong effect on R_x, which will vary as d_o^4. To illustrate the importance of d_o, a 200 MHz resonator with $d_o = 1$ μm, $t = 2$ μm, and $V_P = 20$ V has an $R_x = 286$ MΩ, which is excessively high, especially at RF frequencies. If the gap is reduced to 100 nm while maintaining the other parameters, R_x decreases to 29 kΩ—strong justification for a disk resonator fabrication technology capable of realizing submicron lateral electrode-to-resonator gaps, such as that described in Section V.

Fig. 7 also includes element values corresponding to the 13.7-μm-radius, 2-μm-thick disk micromechanical resonator measured in Section VI, assuming $V_P = 30$ V.

IV. Measurement Theory and Techniques

Several different approaches to measuring the frequency response of the disk structure are available [13]. Sections IV-A–D present four such techniques and discuss their theory, advantages, and disadvantages.

A. One-Port Measurement

The one-port, direct measurement scheme, depicted in Fig. 8 requires only a single input electrode, and so is applicable to perhaps the largest variety of resonator types. As shown in the figure, a bias-T is utilized in this set-up to allow application of the dc-bias voltage V_P (through inductive coupling) to the conductive disk structure while simultaneously tapping that port via capacitive coupling to obtain the output current. For this set-up, the equivalent electrical circuit for the disk is obtained by shorting Port 1 and Port 2 in Fig. 7, which effectively combines the currents from each electrode, allowing the maximum output current among the different measurement methods described here. In particular, note that the total series motional resistance R_x decreases by $4\times$ over that of a single port R_{xn}, because the total η has doubled. In a one-port configuration, the equivalent circuit for the disk reduces to that of Fig. 9.

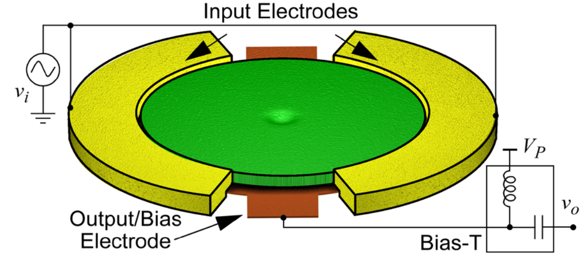

Fig. 8. Perspective view of a one-port measurement setup. (Color version available online at http://ieeexlpore.ieee.org.)

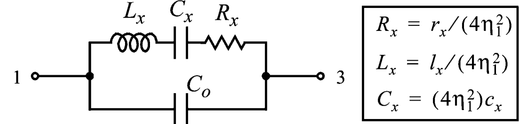

Fig. 9. Equivalent circuit for the radial-contour mode disk operated as a one-port.

Unfortunately, the relatively large motional current provided by a one-port configuration results in very little gain in measurement resolution, because this motional current must compete with parasitic currents running through the static electrode-to-resonator capacitor C_o, which is in a feedthrough position when the resonator is used as a one port. More specifically, referring to Fig. 7 and (17), the admittance of the device at resonance is given by

$$Y_{\text{in}} = \frac{1}{R_x} + j\omega_o C_o \tag{18}$$

where C_o is now equal to $C_{o1} + C_{o2}$—double its original two-port value. For sufficiently large values of $\omega_o C_o$ relative to $1/R_x$, the capacitance term dominates, resulting in a feedthrough current that effectively masks the motional current derived from R_x. Furthermore, C_o creates a parallel-resonance at the frequency given by

$$f_p = f_o\sqrt{1 + \frac{C_x}{C_o}} = \frac{\sqrt{C_o + C_x}}{2\pi\sqrt{C_o C_x L_x}} \tag{19}$$

where $C_x = \eta^2 c_x$ and $L_x = l_x/\eta^2$. C_o is typically much larger than C_x, so f_p is often very close to the series resonance frequency $f_o = 1/2\pi\sqrt{C_x L_x}$ and can distort the measured signal, shifting the resonance peak, altering the passband, and making the true performance parameters of the resonator difficult to extract, especially the device Q.

To improve the ratio of $\omega_o C_o$ to $1/R_x$, the electromechanical coupling coefficient η should be increased. According the previous section, gap spacing is the most viable parameter to optimize. Hence, in subsequent device generations, the gap can be scaled in order to reduce the ratio between R_x and the impedance of C_o, $(R_x/(1/\omega C_o))$, which is proportional to d^3. In order to ensure a measurable peak of at least 6 dB, this impedance ratio should be 0.5 or less.

Section VI will present actual measurements to better illustrate the above issues with the one-port measurement scheme.

B. Two-Port Measurement

If a second electrode is available, the two-port measurement scheme depicted in Fig. 1 can overcome the problems posed by

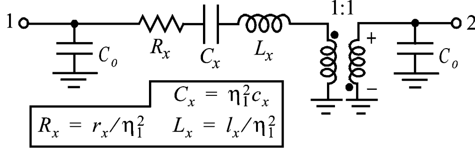

Fig. 10. Equivalent circuit for the radial-contour mode disk resonator configured as a two-port.

C_o in a device with sub-optimal gap spacing. In this scheme, the dc bias is applied directly to the structure, without the need for a bias-T. The ac input signal is applied to one of the electrodes, and the output motional current is detected from the other. With the electrode layout depicted, this excitation scheme results in a nonsymmetric force used to excite a symmetric mode shape. However, so long as the force is applied at the frequency corresponding to the symmetric mode, the resultant vibration will assume the correct mode shape with only slight distortion.

In going from a single electrode that completely surrounds the disk to a split of two smaller electrodes, the motional current magnitude is now constrained to its single-port value, which is $4\times$ smaller than when the device is configured as a one-port. In other words, η is reduced by a factor of two relative to the one-port case, because the electrode area has been halved. Thus, at first glance, the two-port measurement scheme of Fig. 1 does not seem favorable versus the one-port counterpart of Fig. 8.

However, as in the one-port case, series motional resistance is not the only governing factor; rather, parasitic feedthrough capacitance, again, plays an overwhelming role. Examining the schematic in Fig. 7, the body Port 3, to which the dc-bias V_P is connected, corresponds to an AC ground. This splits the static capacitance that originally fed through from input-to-output in the one-port configuration into two, and shunts the dangling ends of these capacitors to ground. The equivalent circuit for the disk then becomes as in Fig. 10, where the feedthrough capacitor that existed in the one-port configuration of Fig. 8 has effectively been removed. With the detrimental effects of a feedthrough C_o negated, the two-port scheme of Fig. 1 enables a cleaner measure of resonator performance than the one-port scheme of Fig. 8, despite a $4\times$ reduction in output current magnitude. The degree of improvement attainable will be quantified more clearly in Section VI via actual measurements.

C. Mixing Measurement

Even with separate input and output electrodes, feedthrough currents between the two electrodes may still exist (e.g., through the substrate, or through bond wires) that can mask the motional current. So there may be a need to do more than just suppress feedthrough currents, but also attempt to move them aside; i.e., to move them away or separate them from the motional current. One approach to separating these currents in the frequency domain is to harness the nonlinear voltage-to-force transfer function of the disk resonator's capacitive transducer in order to excite it into resonance using a set of input frequencies different from its resonance frequency [14]. In this regard, the inherent square-law nonlinearity of the disk's capacitive transducer can be gainfully employed to mix out-of-band electrical input signals to a force acting at the resonance frequency. This setup is similar to that in Fig. 8, but with an ac excitation v_i given by

$$v_i = V_1\cos\omega_c t + V_2\cos[(\omega_c+\omega_o)t] + V_3\cos[(\omega_c-\omega_o)t] \quad (20)$$

where ω_c is a carrier frequency much higher than the resonance frequency ω_o. This input generates a force on the resonator given by

$$F_{\text{mix}} = \frac{1}{2}(V_P - v_i)^2\frac{\partial C_o}{\partial r} \quad (21)$$

where $\partial C_o/\partial r$ is the change in input electrode-to-resonator overlap capacitance per unit displacement approximately given by [8]

$$\frac{\partial C_o}{\partial r} \approx \frac{C_o}{d_o} \quad (22)$$

Substituting (20) and (22) into (21), results in a series of forces acting at various frequencies; the most important of which acts at the resonance frequency ω_o with a magnitude given by

$$|F_{\text{mix}}| = \frac{C_o V_1(V_2+V_3)}{2d_o}. \quad (23)$$

This in-band force is effectively multiplied by the Q of the resonator resulting in vibration at the resonance frequency and output motional current separated from drive parasitics in the frequency domain. Because the inputs are at a much greater frequency than ω_o, they may easily be filtered, resulting in an output current due completely to motion of the resonator with no parasitic effects from C_o.

D. Alternative RF/LO Mixing Measurement

An alternative mixing technique, similar to that discussed above, is possible using an RF/LO (local oscillator) scheme as described in [14]. In this case, a two-port configuration is used, but v_i is replaced with

$$v_i = V_{\text{RF}}\cos\omega_{\text{RF}} t \quad (24)$$

and an additional input signal v_{LO} is applied on top of the dc-bias V_P to the bias port through a bias-T such that

$$v_{\text{LO}} = V_{\text{LO}}\cos\omega_{\text{LO}} t \quad (25)$$

$$\omega_o = \omega_{\text{RF}} - \omega_{\text{LO}}. \quad (26)$$

The mixing of the two signals results in a force acting at the resonance frequency ω_o given by

$$|F_{\text{mix}}| = \frac{1}{2}\frac{C_o}{d_o}V_{\text{LO}}V_{RF} \quad (27)$$

and an output current at that frequency with feedthrough only at ω_{LO} and ω_{RF} (through parasitics), both far away from ω_o.

More details on each of the above mixing measurement techniques are presented in Section VI, which provides the specific setups for actual experimental measurement.

V. Fabrication

The need for submicron, high-aspect ratio, lateral electrode-to-resonator gaps in the disk resonator of Fig. 1 constitutes the most daunting requirement on the fabrication technology. Although 100 nm lateral gaps have been achieved previously in μmechanical structures using e-beam lithography [15], this approach was found to be both time consuming and costly. In addition, if impedances on the order of 50 Ω are desired, 100 nm gaps may not be sufficient, and even smaller gaps on

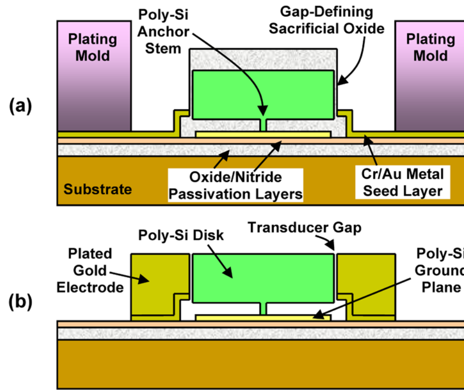

Fig. 11. Process cross section for the disk resonator. (a) A conformal sidewall oxide and electroplating mold are added to an otherwise conventional surface micromachining process. (b) Electrode is plated between the PR mold and sidewalls, then the structure is released. (Color version available online at http://ieeexlpore.ieee.org.)

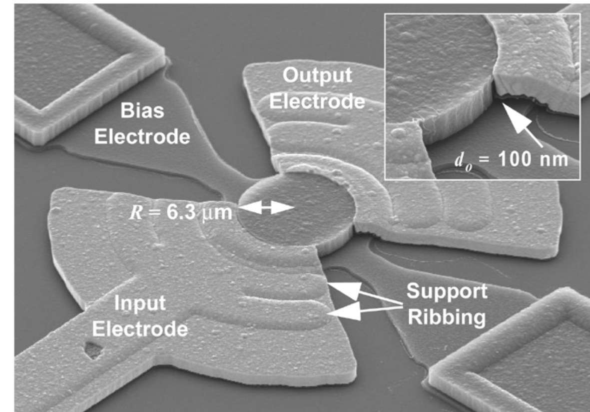

Fig. 12. SEM of a fabricated 433 MHz (first mode) disk resonator.

the order of 30 nm may in fact be desired [14]. To avoid the limitations of lithography and dry etching, the fabrication technology of this work combines surface micromachining, metal electroplating, and a sacrificial sidewall-spacer technique to achieve lateral polysilicon disk resonators with metal electrodes and submicron lateral electrode-to-resonator gaps, all without the need for aggressive lithographic or etching capability.

Fig. 11 presents a pair of cross sections from the process flow. The initial process steps are identical to those used in previous polysilicon surface micromachining processes [12] to achieve a cross-section where a 2-μm-thick polysilicon layer, patterned to form the disk structure, is temporarily supported by a 500 nm first sacrificial oxide layer, over a 1–10 Ω-cm silicon substrate with patterned polysilicon interconnect and ground plane lines. Instead of releasing the structure at this point, as would be done in a conventional surface micromachining process, this process continues with the conformal deposition of 100 nm of LPCVD oxide to cover the sidewalls of the structure and serve as the gap-defining sacrificial layer. Next, the sidewall sacrificial and the underlying oxide are etched (away from the disk) to open anchors to the substrate passivation and interconnect layers, and a Cr/Au metal seed layer is evaporated onto the wafer and removed from the top and sides of the structure in order to prevent plating in these areas during a later step. A thick photoresist mold is then deposited and patterned to define the electrodes, resulting in the cross-section of Fig. 11(a). This is followed by plating of the Au electrodes, using the PR as one portion of the mold and the sidewall of the structure (i.e., of the disk) as the other, plating directly against the sidewall sacrificial layer. The PR and seed layer are then stripped, and the structure is released in 48.8 wt.% hydrofluoric acid (HF) to achieve the final cross-section shown in Fig. 11(b). The result: A disk suspended over the substrate by a single anchor at its center, and separated from the plated electrodes by a thin air gap defined by the sacrificial layer.

Early trials of the electrode plating portion of this process suffered from adhesion problems, whereby the Cr/Au seed layer used for plating delaminated after the final HF release etch, rendering devices electrodeless and untestable. Careful diagnosis revealed that the source of the problem actually originated during the Cr/Au seed layer patterning step. In particular, wet etching of the Cr adhesion layer while in contact with the Au gave rise to significant undercutting of the Cr in conjunction with a very nonuniform etch rate, perhaps due to stresses at the interface between the Cr and Au. Although adhesion appeared good immediately following seed layer removal, the subsequent HF release would attack the already weakened interface and lift-off the metal patterns. Switching to a Cl_2/O_2 plasma to etch the Cr layer during seed layer patterning completely eliminated the problem, allowing firmly anchored metal electrodes at the end of the process. To further ensure adequate adhesion of the metal layer, the electrodes were also bolstered by ribbing, formed by patterning the electrode polysilicon layer directly underneath the plated areas. This ribbing adds lateral support to the metal by creating an interlocking topography on which the plated electrode rests, helping to improve adhesion to the substrate.

The minimum gap thickness in this process is limited only by the ability to control the thickness of a conformally deposited oxide film, and is independent of lithography and etching. While small submicron lateral gaps would seem challenging to wet etch, the diffusion path is relatively short compared to the distance required to fully undercut the resonator to the anchor post, and it is this undercut distance which determines the total release time. Release times vary from 10 min for a 6.3-μm-radius disk with a 0.5-μm-thick underlying sacrificial oxide, to 30 min for a 36.1-μm-radius disk with the same underlying sacrificial oxide thickness. If shorter release times are required, the thickness of the underlying oxide can be increased to improve transport and reduce release times to a degree. In total, the process requires five masks; three for the typical 2-poly surface micromachining process and two additional masks to form the metal electrode. A more thorough treatment of this process technology is given in [16].

Fig. 12 presents a scanning electron micrograph (SEM) of a fabricated and released 433 MHz disk resonator, and the inset shows a close-up of this same resonator, offering a clearer view of its 100 nm electrode-to-resonator gap. In the inset, the electrode appears to rest at an angle compared to the resonator. However, this is simply an artifact of attempting to electroplate into a sharp corner, and when the resonator is removed, it can be seen that the electrode conforms very well to the resonator away from that corner. The aforementioned support ribbing underneath the plated electrodes is also clearly visible in the SEM as ridges along the electrodes.

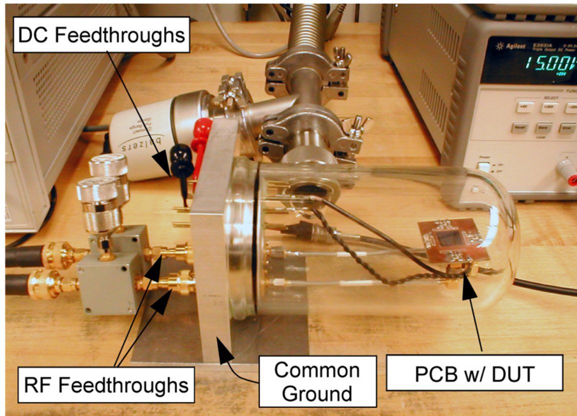

Fig. 13. Photograph of the custom-built vacuum chamber used to measure micromechanical disk resonators. (DUT = Device Under Test.) (Color version available online at http://ieeexlpore.ieee.org.)

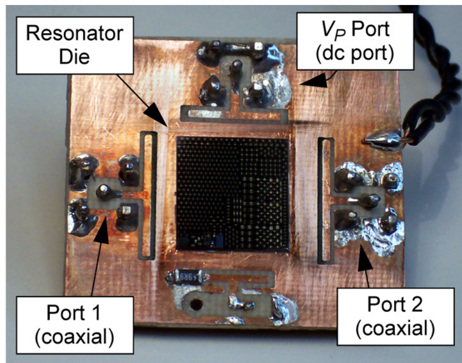

Fig. 14. Photograph of the pc board housing the mounted disk resonator die during testing. (Color version available online at http://ieeexlpore.ieee.org.)

VI. Experimental Results

Each of the measurement techniques detailed in Section IV were evaluated by applying them to the characterization of a variety of disk resonators at a pressure of approximately 50 μTorr supplied by a custom built vacuum chamber, unless otherwise noted. Fig. 13 presents a photo of the vacuum chamber, comprised of a glass bulb that seals over an o-ring-sealed aluminum plate. As indicated, the aluminum plate is embedded with a variety of dc and coaxial feedthroughs that provide electrical bias and excitation access to pc-board-mounted devices within the vacuum chamber. Fig. 14 presents a photo of the custom-designed test pc-board, onto which a die containing disk resonators is silver epoxied to a copper ground shield. Device bond pads (shown in Fig. 15) are wire-bonded to copper traces on the board that connect its dc-bias and input/output pads to SMA connectors and lines that feed through the aluminum plate.

In comparing results obtained using the above set-up with each of the measurement techniques described in Section IV, particular attention was given to the accuracy of the extracted mechanical Q. Since Q is of most interest, here, no attempt was made to match the impedance of the device under test to the measurement instrumentation. One consequence of this is measurement loss due to the impedance-mismatch between the device under test and the measurement instrumentation. For example, if a micromechanical resonator with a series motional resistance of 25 kΩ is driven from a 50 Ω source resistance, and its output fed directly into the 50 Ω input of a network analyzer, a resistive-divider loss of $(50/(50+25\,000+50))\times 2 = -48\,\mathrm{dB}$ ensues (where the factor of 2 accounts for a through calibration). This, of course, is not actual device loss, and the reader should be aware of this. In fact, when used in properly terminated filters as in [12] and [17], losses less than 1 dB are commonly observed, which are consistent with what would be expected, given the very high Q of these resonators.

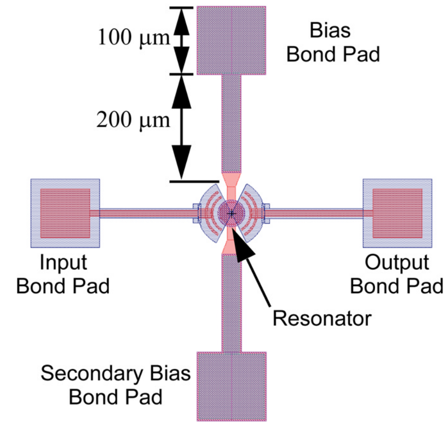

Fig. 15. Layout for the 13.7-μm-radius disk resonator measured in this work, showing the bond pad layout with distances. (Color version available online at http://ieeexlpore.ieee.org.)

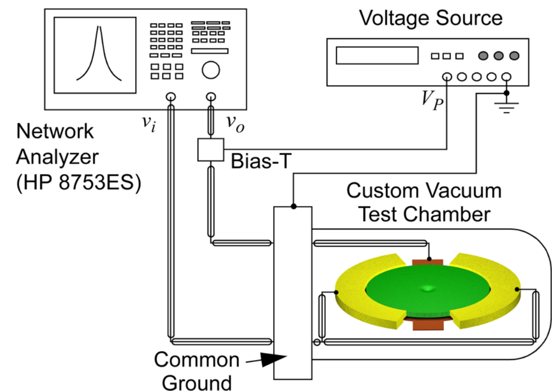

Fig. 16. Test setup for one-port measurement. (Color version available online at http://ieeexlpore.ieee.org.)

A. One and Two-port Measurements

Fig. 16 depicts the test setup for a one-port measurement. Here, the RF-Out port of an HP 8753ES network analyzer is connected directly to both metal electrodes of the resonator inside the test chamber, and the analyzer's RF-In port is connected to the body of the resonator through a bias-T, as is the bias voltage from a dc power supply. Before any measurement is made, a through calibration is first performed, in which the device under test (DUT) is replaced by a short, a measurement is performed, and the network analyzer is baseline corrected against this measurement. Again, no attempt is made to match the resonator to the testing circuit, as doing so would load the device, reducing its Q. As explained above, the large mismatch between the 50 Ω impedance of the test equipment and the resonator $R_x \sim 25$ kΩ results in a rather high, but tolerable, resistive-divider loss of 47 dB in this particular measurement scheme, not to be mistaken for actual device loss.

Fig. 17(a) shows a transmission spectrum obtained from a one-port measurement of a 156 MHz disk resonator along with design parameters and extracted *RLC* element values. Due to the

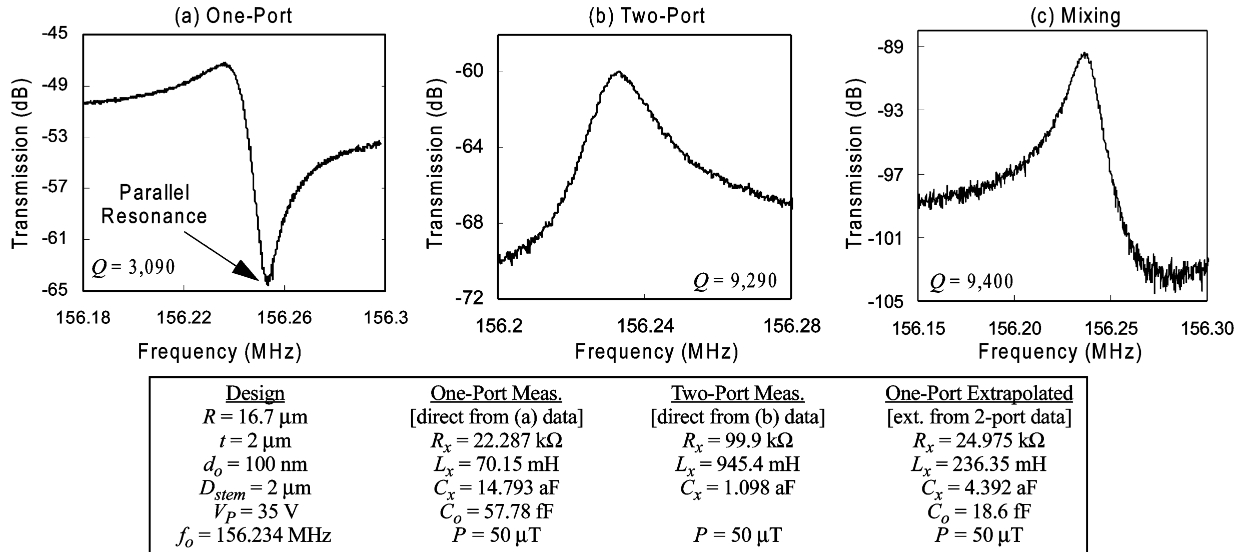

Design	One-Port Meas. [direct from (a) data]	Two-Port Meas. [direct from (b) data]	One-Port Extrapolated [ext. from 2-port data]
$R = 16.7\ \mu m$	$R_x = 22.287\ k\Omega$	$R_x = 99.9\ k\Omega$	$R_x = 24.975\ k\Omega$
$t = 2\ \mu m$	$L_x = 70.15$ mH	$L_x = 945.4$ mH	$L_x = 236.35$ mH
$d_o = 100$ nm	$C_x = 14.793$ aF	$C_x = 1.098$ aF	$C_x = 4.392$ aF
$D_{stem} = 2\ \mu m$	$C_o = 57.78$ fF		$C_o = 18.6$ fF
$V_P = 35$ V	$P = 50\ \mu T$	$P = 50\ \mu T$	$P = 50\ \mu T$
$f_o = 156.234$ MHz			

Fig. 17. 156-MHz disk resonator spectra showing (a) one-port, (b) two-port, and (c) mixing measurements of the same resonator. The design parameters of the measured resonator are summarized below the plots, as are the equivalent circuits extracted from the measured plots.

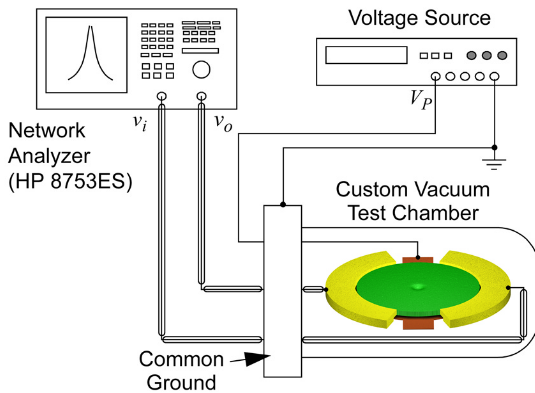

Fig. 18. Test setup for two-port measurement. (Color version available online at http://ieeexlpore.ieee.org.)

presence of a large C_o, the peak height is less than 4 dB above the surrounding feed-through level. The parallel-resonance is also evident as the sharp notch near the series resonance peak. The combination of these effects leads to an extracted Q of 3090.

The test setup for the two-port measurement, shown in Fig. 18, is similar to that of the one-port except that the bias-T is removed, and the dc bias voltage is connected directly to the body of the resonator. The RF-Out port is connected to one metal electrode, and the RF-In port is connected to the other. Fig. 17(b) shows a transmission spectrum of a 156 MHz resonator obtained via the two-port technique. The resistive-divider loss is approximately 12 dB higher, consistent with the $4\times$ increase in R_x and a corresponding $16\times$ decrease in the power measured at the analyzer. However, with reduction of the feed-through capacitance C_o, the peak height has increased to better than 8 dB above the noise floor, while the parallel-resonance has been eliminated. With this more accurate spectrum, the extracted Q is increased to 9290.

With a much more accurate Q value as its base, the equivalent circuit (in column 3 of Fig. 17) extracted from two-port data is much more accurate than that obtained from the one-port data (in column 2 of Fig. 17). In fact, the one-port extracted equivalent circuit does not match the theoretical prediction of Section III, and is actually quite incorrect. For practical purposes, the equivalent circuit for the disk configured as a one-port is better obtained by taking the two-port extracted circuit and modifying it according to the change in electrode-to-resonator overlap, as is done in the column to the far right in Fig. 17, which now gives the correct one-port values. (The values in this column were obtained by adjusting the two-port R_x, L_x, and C_x, by factors of $0.25\times$, $0.25\times$, and $4\times$, respectively, to account for the doubling in electrode-to-resonator overlap in going from the two-port to the one-port configuration. The value of C_o was obtained by matching a circuit simulation using SPICE to the measured one-port data.)

B. Mixing Measurements

Fig. 19 depicts the test setup for a mixed measurement, where the resonator is used once again as a one-port in order to maximize the electrostatic forcing efficiency and the output current, while relying on mixing to circumvent the increase in overlap feedthrough capacitance, as described in Section IV-C. Testing occurs in four steps, outlined in Fig. 19 and denoted by letters in the schematic. First, an IF signal ω_{IF} near the resonance frequency of the device is generated by the network analyzer and mixed via a discrete mixer with a carrier signal ω_c from a signal generator. The resultant Fourier spectrum shown at (A) consists of IF and carrier leakage components and the mixing products. At (B), the input to the resonator, carrier power is re-injected in order to increase signal strength [cf. (23)], and the IF leakage is blocked by a high pass filter. The square-law voltage-to-force nonlinearity in the parallel plate capacitive transducer then remixes the carrier and its sidebands, generating a force component acting at the IF frequency that drives the device at resonance and produces the output spectrum at (C). Because the input electrical signal is completely out-of-band, the resultant IF current is entirely derived from the motion of the resonator with ideally no feedthrough interference at ω_{IF}. At (D), the measurement port, a low-pass filter blocks feed-through components from the carrier and sidebands to prevent overdriving of the network analyzer. A major advantage

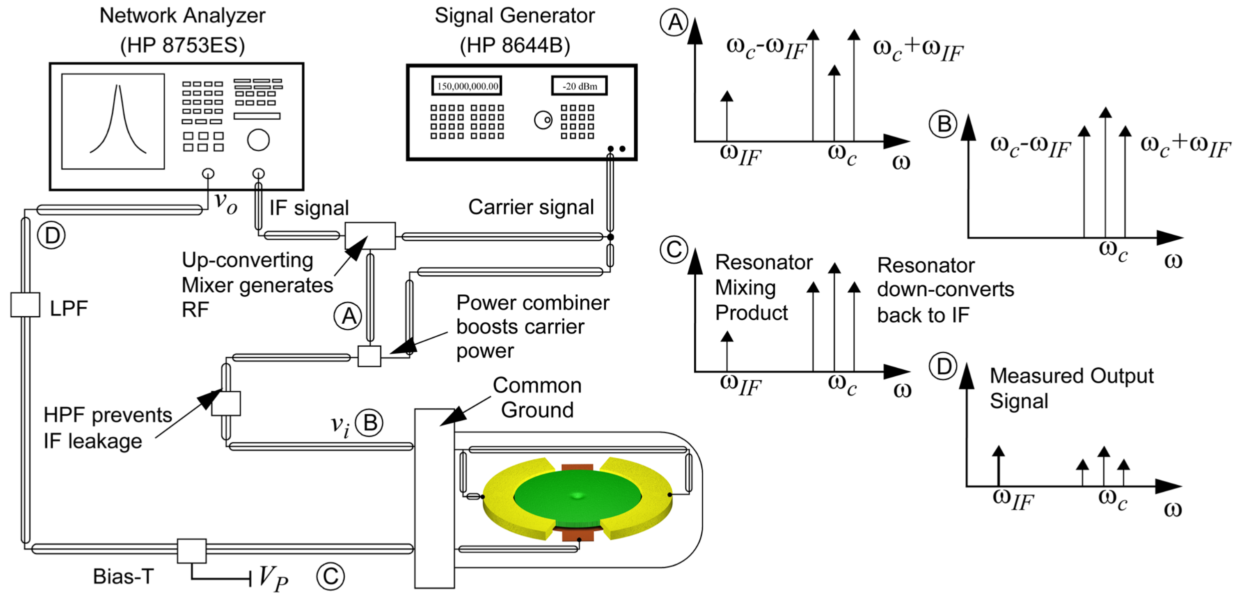

Fig. 19. Test setup for mixing measurement and signal Fourier spectra at various locations in the setup. (Color version available online at http://ieeexlpore.ieee.org.)

of this technique over other mixing techniques [14] is that the output signal is at the drive frequency of the network analyzer, allowing direct measurement on the analyzer. The mixing spectrum in Fig. 17(c), obtained from the same resonator as the one-port measurement but using this mixing technique, shows a peak height greater than 10 dB, and barely any parallel resonance compared with the one-port measurement method, allowing a more accurate Q measurement of 9400.

C. RF/LO Mixing—Overtone Measurements

While the mixing measurement setup in Fig. 19 is very useful for evaluating some hard-to-measure devices, its complexity can lead to some difficulties. Leakage and nonlinearity in each component of the system can contribute to signal degradation, especially as the frequency of interest is increased. For example, if the upconverting mixer or power combiner in the input path of the system are not sufficiently linear, signals at IF can be generated right at the input. This, of course, defeats the main advantage of the above mixing technique, where the use of only off-resonance input signals is the key to eliminating feedthrough at the IF frequency. This is, in fact, the reason for the tiny parallel resonance peak seen in Fig. 17(c).

To circumvent problems due to component nonlinearity, a simpler measurement technique that dispenses with such components is desirable. The RF/LO method described in Section IV-D is such a technique. Fig. 20 presents the test set-up used to implement the RF/LO measurement scheme [14]. Here, a network analyzer or other swept signal source provides the RF signal, while a function generator supplies the LO to the bias port via a bias-T. The output signal is measured on a spectrum analyzer. The disadvantage of this technique is that the spectrum analyzer is not well suited to swept measurements of this sort, requiring a maximum sample-and-hold technique or computer control to capture the necessary data. However, the RF/LO technique, with fewer sources of nonlinearity, is more robust and extensible to higher frequencies.

Fig. 21 shows three spectra obtained via RF/LO measurements from a single 13.7-μm-radius disk resonator operating

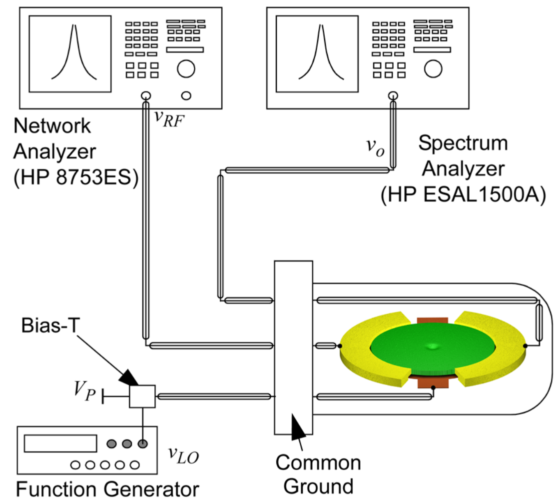

Fig. 20. Test setup for RF/LO measurement. (Color version available online at http://ieeexlpore.ieee.org.)

in the first three radial modes. In the fundamental mode, the resonator operates at 193 MHz with a Q in excess of 23 000. The second mode is at 515 MHz with a Q of approximately 9000, and the third mode is centered at 829 MHz. Unfortunately, for the 829 MHz case, even using this measurement technique, other nonlinearities in the measurement setup begin to dominate, yielding a peak height of just over 2 dB—insufficient to extract the Q. Note that the vertical axis for the RF/LO measurements is given in units of actual power measured at the output port (in dBm) rather than in relative power (dB), as the measurement data is collected on a spectrum analyzer rather than a network analyzer. A variety of resonators have been tested, and for the fundamental mode, the highest frequency measured was 433 MHz for a 6.3-μm-radius disk with a Q of over 4000. Of the resonators measured, the results in Fig. 21 show the best response for the second mode, while the third mode has been measured with Q's as high as 3200 at 317 MHz.

As was mentioned previously, all of the results in Figs. 17 and 21 were obtained with the resonator operating under vacuum

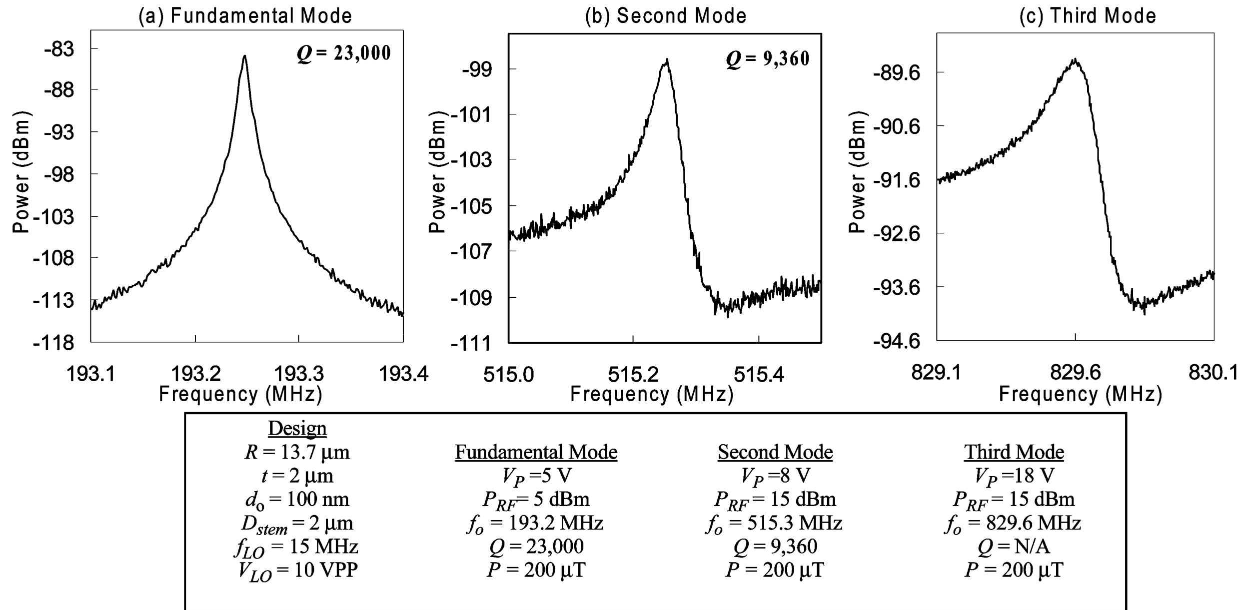

Fig. 21. 13.7 μm radius disk resonator tested in the (a) fundamental, (b) second, and (c) third modes via the RF/LO measurement technique.

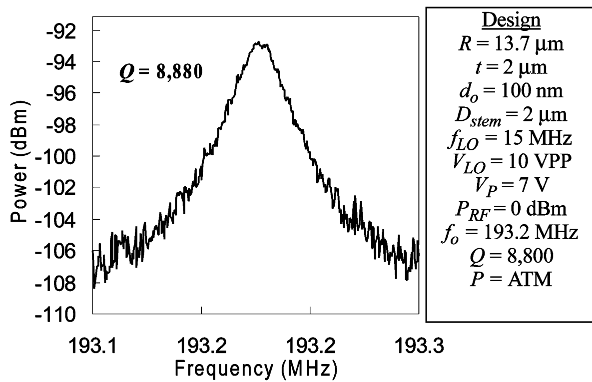

Fig. 22. The resonator of Fig. 21 measured at atmospheric pressure.

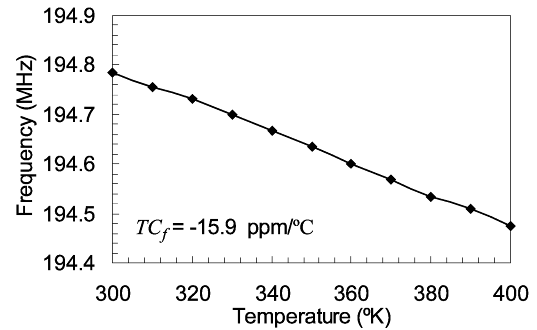

Fig. 23. Plot of resonant frequency versus temperature for a 195-MHz disk resonator similar to that measured in Fig. 21.

pressures of roughly 50 μT, and previous resonators [1], [12], [14] required vacuum in order to obtain acceptable quality factors. The spectrum in Fig. 22 was obtained from the same resonator measured in Fig. 21, but operated in the fundamental mode at atmospheric pressure. The Q remains high at 8880, good enough for many applications. Disk resonators are able to maintain high Q at atmospheric pressure due to their high stiffness in comparison to other types of resonators. In particular, rearranging (11)

$$Q = \frac{k}{c_r \omega_o}. \tag{28}$$

At atmospheric pressure, the damping term c_r is dominated by fluidic air damping, which for comparable vibration amplitudes, acts at roughly the same magnitude in disk resonators as other resonator types. (Note that the disk resonators of this work are driven harder than previous VHF resonators during measurement so as to attain similar vibration amplitudes, in the 1–10 nm range.) With similar air damping—or less, if the disk amplitude is smaller than that of previous resonators—and with an equivalent disk stiffness much larger than previous resonator types [1], [12], [18], (28) correctly predicts a much higher Q for a disk relative to previous VHF designs when operated in air at the same frequency. In effect, the very high stiffness on the order of 3.5 MN/m of a fundamental-mode 13.7 μm-radius, 2 μm-thick disk gives it a peak energy per cycle many times larger than the energy loss per cycle due to air damping, allowing for high Q even at atmospheric pressure.

Because these resonators can perform well in atmosphere, the need for vacuum packaging is eliminated for many applications, removing a significant barrier to the implementation of micromechanical resonators in practical wireless systems.

D. Additional Measurements

Another important resonator performance parameter is the *temperature coefficient of frequency*, or TC_f. In disk resonators, the variation in frequency with temperature is predominantly caused by the thermal expansion of the resonator material and the temperature dependence of Young's Modulus, which typically dominates the temperature response. Fig. 23 shows a measured plot of frequency versus temperature for a 193 MHz disk resonator operated under conditions similar to those in Fig. 21(a). The extracted TC_f is about -16 ppm/°C, which is comparable to that of other micromechanical resonators. The temperature curve is also fairly linear, enabling simpler

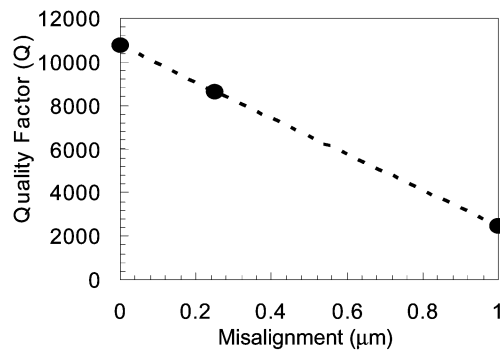

Fig. 24. Plot of the measured Quality factor versus anchor mis-alignment for a 195-MHz disk resonator similar to that measured in Fig. 21. Note that the connecting line is added only to emphasize the general trend of the highlighted data points and does not constitute a rigorous analysis or interpolation of the results.

compensation methods than devices which show nonlinear temperature characteristics, such as quartz crystals [19].

As described in Section V the fabrication process relies on a manual mask alignment to center the resonator on the anchor post. Errors in this alignment can introduce changes in frequency and can degrade the resonator Q. Fig. 24 shows a plot of Q versus anchor post misalignment for a set of three manufactured and measured devices which were intentionally misaligned in layout and had their misalignment confirmed and quantified via SEM measurements. While finite element simulations can provide a clear view of the effects of anchor location on frequency, quality factor is very difficult to simulate accurately, and empirical measurements yield more reliable results. Based on the measured data, clearly even a small misalignment, on the order of only 100 nm, can result in a significant change in resonator performance. Although this data is drawn from a small sample size, the variations in Q are much larger than the typical device-to-device variations, giving strong justification for a self-aligned process such as recently demonstrated in [20]. The process of [20], however, uses polysilicon electrodes, so is not directly compatible with the metal electrode process described here. Adaptation of the process to use metal electrodes is the subject of future work.

A final point of interest is the tunability of disk resonators. Previous micromechanical resonator designs [1], [12], [14] have exhibited some degree of tunability due to the electrical spring constant [21], [22]. However, the tuning range derived from the electrical spring constant is inversely proportional to the stiffness of the resonator; *i.e.*, with increasing stiffness, the effective tuning range is reduced. For example, in a 193 MHz disk resonator such as that measured in Fig. 21(a), the total tuning range as the dc-bias is varied from 0 V to 25 V is only 19 kHz or 0.01%. As such, if necessary, other trimming and tuning techniques will be required to correct for finite fabrication tolerances in these types of resonators.

VII. Conclusion

A laterally vibrating radial contour mode μmechanical disk resonator was presented with a measured fundamental-mode frequency and Q as high as 433 MHz and 4000, respectively. In addition, resonators were demonstrated with Q's as high as 23 000 in the fundamental mode at 193 MHz. Operation in the second overtone was demonstrated at 515 MHz with a Q of 9300, and operation in the third overtone was demonstrated with Q's up to 3200 at 317 MHz and at frequencies up to 829 MHz. Disk resonators were also demonstrated operating at atmospheric pressure with Q's as high as nearly 9000, greatly reducing the need for and cost associated with vacuum packaging. These results push the operating frequencies of micromechanical resonators well into the UHF range and even into the U.S. cellular frequency band. Such performance will enable revolutionary signal processor concepts with substantial potential for lowering power consumption in wireless handsets (e.g., via an RF channel selector at the front-end of a wireless receiver).

Finally, several techniques were demonstrated for the accurate characterization of suboptimal (i.e., research prototype) micromechanical resonators under conditions where parasitic currents may mask resonator motional current. Specifically, two-port and mixing measurement schemes improved the Q of 3090 extracted from a one-port measurement to a much more accurate 9290 at 156 MHz. Such techniques are vital to the rapid evaluation of nonideal, prototype resonators, as they ease design and fabrication constraints for first generation research devices.

References

[1] K. Wang, A.-C. Wong, and C. T.-C. Nguyen, "VHF free-free beam high-Q micromechanical resonators," *J. Microelectromech. Syst.*, vol. 9, no. 3, pp. 347–360, Sep. 2000.

[2] J. R. Clark, W.-T. Hsu, and C. T.-C. Nguyen, "High-Q VHF micromechanical contour-mode disk resonators," in *Tech. Digest, IEEE Int. Electron Devices Meeting*, San Francisco, CA, Dec. 11–13, 2000, pp. 399–402.

[3] X. M. H. Huang, M. K. Prakash, C. A. Zorman, M. Mehregany, and M. L. Roukes, "Free-free beam silicon carbide nanomechanical resonators," in *Dig. of Tech. Papers, the 12th Int. Conf. on Solid-State Sensors & Actuators (Transducers'03)*, Boston, MA, Jun. 8–12, 2003, pp. 342–343.

[4] M. A. Abdelmoneum, M. U. Demirci, and C. T.-C. Nguyen, "Stemless wine-glass-mode disk micromechanical resonators," in *Proc. 16th Int. IEEE Micro Electro Mechanical Systems Conf.*, Kyoto, Japan, Jan. 19–23, 2003, pp. 698–701.

[5] S. Pourkamali and F. Ayazi, "SOI-based HF and VHF single-crystal silicon resonators with sub-100 nanometer vertical capacitive gaps," in *Dig. of Tech. Papers, the 12th Int. Conf. on Solid-State Sensors & Actuators (Transducers'03)*, Boston, MA, Jun. 8–12, 2003, pp. 837–840.

[6] C. T.-C. Nguyen, "Transceiver front-end architectures using vibrating micromechanical signal processors (invited)," in *Dig. of Papers, Topical Meeting on Silicon Monolithic Integrated Circuits in RF Systems*, Sep. 12–14, 2001, pp. 23–32.

[7] ——, "Frequency-selective MEMS for miniaturized low-power communication devices (invited)," *IEEE Trans. Microw. Theory Tech.*, vol. 47, pp. 1486–1503, Aug. 1999.

[8] R. Navid, J. R. Clark, M. Demirci, and C. T.-C. Nguyen, "Third-order intermodulation distortion in capacitively-driven CC-beam micromechanical resonators," in *Technical Digest, 14th Int. IEEE Micro Electro Mechanical Systems Conference*, Interlaken, Switzerland, Jan. 21–25, 2001, pp. 228–231.

[9] J. R. Vig and Y. Kim, "Noise in microelectromechanical system resonators," *IEEE Transactions on Ultrasonics, Ferroelectrics, and Frequency Control*, vol. 46, pp. 1558–1565, 1999.

[10] M. Onoe, "Contour vibrations of isotropic circular plates," *J. Acoust. Soc. Amer.*, vol. 28, no. 6, pp. 1158–1162, 1956.

[11] R. A. Johnson, *Mechanical Filters in Electronics*. New York: Wiley, 1983.

[12] F. D. Bannon III, J. R. Clark, and C. T.-C. Nguyen, "High frequency micromechanical filters," *IEEE J. Solid-State Circuits*, vol. 35, pp. 512–526, Apr. 2000.

[13] J. R. Clark, W.-T. Hsu, and C. T.-C. Nguyen, "Measurement techniques for capacitively-transduced VHF-to-UHF micromechanical resonators," in *Dig. of Tech. Papers, the 11th Int. Conf. on Solid-State Sensors & Actuators (Transducers'01)*, Munich, Germany, Jun. 10–14, 2001, pp. 1118–1121.

[14] A.-C. Wong, H. Ding, and C. T.-C. Nguyen, "Micromechanical mixer + filters," in *Tech. Digest, IEEE Int. Electron Devices Meeting*, San Francisco, CA, Dec. 6–9, 1998, pp. 471–474.

[15] J. W. Weigold, A.-C. Wong, C. T.-C. Nguyen, and S. W. Pang, "A merged process for thick single crystal Si resonators and conventional BiCMOS circuitry," *J. Microelectromech. Syst.*, vol. 8, no. 3, pp. 221–228, Sep. 1999.

[16] W.-T. Hsu, J. R. Clark, and C. T.-C. Nguyen, "A sub-micron capacitive gap process for multiple-metal-electrode lateral micromechanical resonators," in *Tech. Digest, 14th Int. IEEE Micro Electro Mechanical Systems Conference*, Interlaken, Switzerland, Jan. 21–25, 2001, pp. 349–352.

[17] K. Wang and C. T. C. Nguyen, "High-order medium frequency micromechanical electronic filters," *J. Microelectromech. Syst.*, vol. 8, pp. 534–556, Dec. 1999.

[18] W. C. Tang, T.-C. H. Nguyen, and R. T. Howe, "Laterally driven polysilicon resonant microstructures," *Sens. Actuators*, vol. 20, pp. 25–32, 1989.

[19] M. E. Frerking, *Crystal Oscillator Design and Temperature Compensation*. New York: Van Nostrand Reinhold, 1978.

[20] J. Wang, Z. Ren, and C. T.-C. Nguyen, "Self-aligned 1.14-GHz vibrating radial-mode disk resonators," in *Dig. of Tech. Papers, the 12th Int. Conf. on Solid-State Sensors & Actuators (Transducers'03)*, Boston, MA, Jun. 8–12, 2003, pp. 947–950.

[21] H. Nathanson, W. E. Newell, R. A. Wickstrom, and J. R. Davis Jr, "The resonant gate transistor," *IEEE Trans. Electron Devices*, vol. ED-14, pp. 117–133, Mar. 1967.

[22] R. T. Howe and R. S. Muller, "Resonant microbridge vapor sensor," *IEEE Trans. Electron Devices*, vol. ED-33, pp. 499–506, 1986.

John R. Clark (S'96–M'03) received the B.S., M.S., and Ph.D. degrees in electrical engineering from the University of Michigan, Ann Arbor, in 1996, 1998, and 2003, respectively.

Upon entering graduate school, he was awarded both the NSF Graduate Research Fellowship and the National Defense Science and Engineering Graduate Fellowship. His doctoral work included fundamental efforts in the field of RF micromechanical resonators, micromechanical filters, and RF MEMS fabrication processes, including ground-breaking efforts to extend the useful frequency range of MEMS resonators. He is currently employed as a Senior MEMS Engineer for Discera, Inc., Ann Arbor, MI. At Discera, he continues his work on micromechanical filters as well as contributing to the design and production of novel timekeeping products, creating innovative RF MEMS technologies to meet the needs of wireless and consumer electronics industry partners.

Wan-Thai Hsu (S'98-M'01) received the B.S. and M.S. degrees from the National Tsing-Hua University, Taiwan, and the Ph.D. degree in 2001 from the University of Michigan, Ann Arbor, all in electrical engineering. His doctoral work focused on the frequency stability, reliable design, and robust manufacturing of high-*Q* micromechanical resonators, and was instrumental towards the successful realization of vibrating RF MEMS products being commercialized by Discera, Inc., the company he soon joined in 2001.

At Discera, he presently serves as Chief Science Officer, where he leads a team on pushing resonator technologies from research to commercialization. He also serves as the Principal Investigator for a National Institute of Standard and Technology (NIST) Advanced Technology Program (ATP) contract titled "Fully Integrated Giga Hertz Receivers." He is a pioneer in micromechanical resonator research and development for applications ranging from RF communications, timekeeping, and low-power wireless sensors. He currently holds three U.S. patents and has three patents pending.

Mohamed A. Abdelmoneum (S'99–M'05) received the B.Sc. degree from Alexandria University, Alexandria, Egypt, in 1994 in electrical communications and electrophysics. He received the M.Sc. and Ph.D. degrees from the University of Michigan, Ann Arbor, in 2000 and 2005, respectively, both in electrical engineering and computer science.

He worked as a Field Engineer in Schlumberger Wire Line and Testing between January and May 1996. He then joined the faculty of the University of Tanta, Tanta, Egypt, as a Lecturer Assistant in the Department of Mathematics and Basic Sciences, where he worked on wavelets and their application to the solution of differential equations. In 1998, he joined the Radiation Laboratory at the University of Michigan, Ann Arbor, where he worked on computational electromagnetics and its application to antenna design, radomes, frequency selective surfaces and electromagnetic computability. In 2001, he switched to the Solid State Electronics Lab of the University of Michigan, where he worked on vibrating micromechanical resonators and filters, the subject of his doctoral thesis. His thesis work explored resonators capable of retaining high *Q*'s under varying environmental conditions and developed methods for laser-assisted post fabrication trimming of micromechanical resonators and filters. He is currently with the Portland Technology Development Automation group at Intel Corporation, Hillsboro, OR, where he is working on yield analysis systems.

Clark T.-C. Nguyen (S'90–M'95–SM'01) received the B.S., M.S., and Ph.D. degrees from the University of California at Berkeley in 1989, 1991, and 1994, respectively, all in electrical engineering and computer sciences.

In 1995, he joined the faculty of the University of Michigan, Ann Arbor, where he is presently an Associate Professor in the Department of Electrical Engineering and Computer Science. His research interests focus upon microelectromechanical systems (MEMS) and include integrated micromechanical signal processors and sensors, merged circuit/micromechanical technologies, RF communication architectures, and integrated circuit design and technology. From 1995 to 1997, he was a Member of the National Aeronautics and Space Administration (NASA)'s New Millennium Integrated Product Development Team on Communications, which roadmapped future communications technologies for NASA use into the turn of the century. In 2001, he founded Discera, Inc., a company aimed at commercializing communication products based upon MEMS technology, with an initial focus on the very vibrating micromechanical resonators pioneered by his research in past years. He served as Vice President and Chief Technology Officer (CTO) of Discera until mid-2002, at which point he joined the Defense Advanced Research Projects Agency (DARPA) on an IPA, where he is presently the Program Manager of the MEMS, Micro Power Generation (MPG), Chip-Scale Atomic Clock (CSAC), MEMS Exchange (MX), Harsh Environment Robust Micromechanical Technology (HERMIT), Micro Gas Analyzers (MGA), Radio Isotope Micropower Sources (RIMS), RF MEMS Improvement (RFMIP), Navigation-Grade Integrated Micro Gyroscopes (NGIMG), and Micro Cryogenic Coolers (MCC) programs, in the Microsystems Technology Office of DARPA.

Prof. Nguyen received the 1938E Award for Research and Teaching Excellence from the University of Michigan in 1998, an EECS Departmental Achievement Award in 1999, the Ruth and Joel Spira Award for Teaching Excellence in 2000, and the University of Michigan's 2001 Henry Russel Award. Among his publication accolades are the 2004 DARPA Tech Best Technical Presentation Award, the Best Invited Paper Award at the 2004 IEEE Custom Integrated Circuits Conference, and together with his students, the Best Student Paper Award in Category 1 at the 2005 Joint IEEE Frequency Control/Precise Time and Timing Interval (PTTI) Symposium, the Best Paper Award in the Frequency Control Category at the 2004 IEEE Ultrasonics, Ferroelectrics, and Frequency Control Symposium, and the Roger A. Haken Best Student Paper Awards at the 1998 and 2003 IEEE International Electron Devices Meetings. To date, he has organized and chaired a total of 35 IEEE and DARPA workshops.